Analysis and Enhancement of Low Voltage Ride-through Capability of Brushless Doubly Fed Induction Generator

Sajjad Tohidi, Hashem Oraee, *Senior Member, IEEE,* Mohammad Reza Zolghadri, *Member, IEEE,* Shiyi Shao, *Member, IEEE,* and Peter Tavner, *Senior Member, IEEE*

***Abstract*— This paper discusses the dynamic behavior of the brushless doubly fed induction generator during the grid faults which lead to a decrease in the generator's terminal voltage. The variation of the fluxes, back EMFs and currents are analyzed during and after the voltage dip. Furthermore, two alternative approaches are proposed to improve the generator ride-through capability; using crowbar and series dynamic resistor circuits. Appropriate values for their resistances are calculated analytically. Finally, the coupled circuit model and the generator's speed and reactive power controllers are simulated to validate the theoretical results and the effectiveness of the proposed solutions. Moreover, experiments are performed to validate the coupled circuit model used.**

***Index Terms*—Brushless Doubly Fed Induction Generator, feasibility region, ride-through, voltage dip**

NOMENCLATURE

V, I	Amplitudes of the voltage and current
v, i	Instantaneous values of the voltage and current
ψ	Flux
p	Number of poles
N_r	Number of rotor loops (nests)
ω	Angular speed
ω_n	Natural speed
f	Frequency
R	Winding resistance
L	Winding self inductance
L_{1r}	Coupling inductance between power winding and rotor
L_{2r}	Coupling inductance between control winding and rotor
Q	Reactive power
T	Torque
J	Moment of inertia
B	Friction coefficient
$\max\{\ \}$	Maximum value

Subscripts

$1,2,r$	Power winding, control winding and rotor
e,m	Electrical and mechanical
cr	Crowbar
c	DC link
d,q	Direct and quadrate axis of the synchronously rotating reference frame
rated	Rated value
sat	Saturated value
$0, f$	Pre-fault and fault-on values

Manuscript received August 5, 2011. Accepted for publication March 3, 2012.

S. Tohidi, H. Oraee, and M. R. Zolghadri are with the Department of Electrical Engineering, Sharif University of Technology, Tehran, 11365-8639 Iran (e-mail: stohidi@ee.sharif.ir, oraee@sharif.edu, zolghadr@sharif.edu).

S. Shao was with the Engineering Department, University of Cambridge, Cambridge, CB3 0FA UK (e-mail: cantabshaoshiyi@hotmail.com)

P. Tavner is with the School of Engineering and Computing Sciences, Durham University, Durham, DH1 3LE UK (e-mail: Peter.Tavner@durham.ac.uk).

I. INTRODUCTION

WIND power has become an important source of renewable energy in a number of countries around the world, including Denmark, Germany and Spain. Therefore, connection of wind farms to the grid and their dynamic behavior under different grid conditions has become an important issue in recent years and new grid codes have been introduced [1], [2]. One of the most important issues relating to grid codes is the ride-through capability of wind farms during voltage dips due to grid faults. Based on these code requirements, wind turbine generators must remain connected to the grid and actively contribute to the system stability during various grid fault scenarios that result in a decrease in the generator terminal voltage. Moreover, wind turbine generators should have the ability during the faults to supply reactive power, in order to increase voltage level. In addition, they should supply active and reactive power immediately after fault clearance to support the network frequency and voltage, respectively.

The majority of recently installed large wind turbines incorporate the doubly fed induction generator (DFIG) with a partially-rated converter. This configuration has the advantages of flexible control of the rotor speed and power factor with a fractionally-sized converter with consequent

reduced cost and relatively low investment. This, however, has the disadvantage of reduced reliability, requiring more maintenance due to the use of brushes and slip-rings [3]. However, there are some alternatives to achieve brushless and variable speed operation. For instance, a constant-frequency machine with a varying/variable speed has been proposed for wind power plants [4]. Another alternative is the brushless doubly fed machine (BDFM). The BDFM, or brushless doubly fed induction generator (BDFIG), maintains all the benefits of the DFIG but without brushes and slip-rings and hence achieving higher reliability and lower operational cost.

Although the converter rating and operation of the BDFM is similar to the DFIG, there are some structural differences between them. The BDFM uses a cage rotor with a special structure, while wound rotor is used in the DFIG. In addition, the BDFM has two windings in the stator. It has been shown that the output of a BDFM is less than a conventional induction machine with the same volume of active material under similar operating conditions [5]. It means that the BDFM would be larger in size than a DFIG with the same rating. But, omitting the brush-gear and slip rings and also the possibility of a stage reduction in the gear-box of wind turbines with BDFM – due to its lower typical rotor speed – can decrease its overall volume and costs. However, there is a need to manufacture a wind turbine with a large-size BDFM and compare its electrical, mechanical and economic parameters with the existing DFIG-based wind turbines. Because of the aforementioned advantages of BDFM, it has great potential for wind power generation, particularly offshore application where maintenance time is at a premium, and for limited speed range variable pump drives [6].

However, in order to realize its commercial promises, dynamic behavior and ride-through capability of BDFM has to be assessed. Several papers have been published relating to BDFM modeling and control. The equivalent circuit is suggested and experimentally validated in [7]. Using this model, performance analysis is carried out and some relations for the active and reactive powers of BDFM are proposed in [5]. A rotor flux-oriented control algorithm is evaluated for the BDFM in [8]. In [9], a unified reference frame *dq* model for BDFM is proposed and verified experimentally. Using this model, a vector control scheme is developed, including experimental implementation in [10]. A BDFM-based drive using a fractionally rated unidirectional converter is proposed and implemented in [11]. Also, the stator flux-oriented control design is developed and implemented for a BDFM in [12]. Another vector model with experimental validation is suggested in [13]. But, the most detailed and precise model using coupled circuits, is developed and described in [14].

Generally, two groups of alternatives have been introduced to improve ride-through and transient capability of DFIG wind turbines. The first group includes appropriate linear or nonlinear controllers [15]-[17]. The second group employs various devices and circuits to achieve this goal, a number of which use FACTS devices [19], supercapacitor energy storage [20], a series grid-side converter [21], crowbar and static transfer switches [22], energy capacitor systems [23], series dynamic resistors (SDR) [24] or dynamic voltage restorers [25], [26]. In addition, in some papers, such as [27], DFIG modeling for ride-through analysis is studied.

But, BDFM ride-through capability has not yet been studied in the literature. For instance, in [28] a brief discussion on ride-through capability is given without any suggestion to improve it. This paper intends to fill this gap and analyzes the dynamic behavior of the BDFIG during and after a three phase voltage dip on its terminals and proposes two effective improvements.

In Section II a brief description on structure of BDFM, fundamentals of operation and its dynamic model is presented. In Section III, the variations of fluxes, EMFs and currents are analyzed during voltage dips using the *dq* model. In Section IV, based upon this analysis, two solutions to enhance ride-through capability of the machine are proposed. Finally, in Section V, the validity of a coupled-circuit model of BDFIG, used for simulation, is checked via comparison with experimental results and the predicted variation of fluxes, EMFs and currents are verified by simulation. Hitherto this paper has talked of the BDFM, however in the following the generating mode of the machine is studied, and hence the abbreviation BDFIG will be used.

II. BDFIG MODELING

The BDFIG has two, three-phase windings in its stator, namely the power winding (PW) and control winding (CW), as shown in Fig. 1. To avoid direct coupling between the two windings, the pole pair numbers must differ by an integer [14].

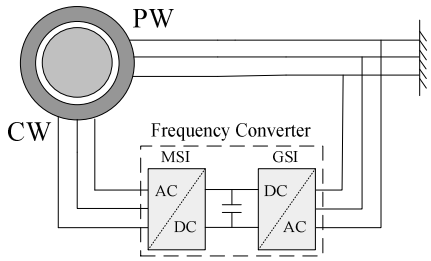

Fig. 1. The BDFIG Structure

Furthermore, in order to reduce asymmetrical electromagnetic forces on the rotor, that pole pair difference should be greater than one [14], that is:

$$|p_1 - p_2| \rangle 1 \tag{1}$$

The PW is connected directly to the grid and therefore operates at grid frequency producing an MMF in the air gap rotating at this frequency. Most of the power will be transferred between the BDFIG and grid via this winding. The CW is connected to grid via a bi-directional partially-rated frequency converter controlling the rotor speed and reactive power supplied or absorbed by the machine [10], [12]. The frequency converter consists of two back-to-back voltage source inverters. The inverter connected to the CW, or the machine-side inverter (MSI), controls the CW current and due to cross-coupling between the CW and PW, affects the PW current. The grid side inverter (GSI) controls the DC link voltage. Its free capacity can also be used to support the

BDFIG terminal voltage by supplying or absorbing reactive power.

The rotor windings are closed upon themselves and hence, no brush or slip-ring is required. The number of loops or poles, N_r, in the rotor winding is chosen to produce cross-coupling between PW and CW [29], that is:

$$N_r = \frac{p_1 \pm p_2}{q} \tag{2}$$

In order to increase N_r and consequently decrease rotor leakage inductance, q is selected equal to 1 and the positive sign is preferred [29]. Hence,

$$N_r = p_1 + p_2 \tag{3}$$

Furthermore, the number of loops in each pole is increased by distributing each loop in several slots to decrease the rotor leakage flux. The most common structure for the rotor winding to date is called the "nested loop" arrangement, as shown in Fig. 2. As can be seen, the nested loop rotor consists of several nests, each representing one rotor circuit containing several loops. Due to the special design of the rotor, various modes of machine operation are obtained.

Fig. 2. Nested loop rotor of the D180 BDFIG

The most interesting mode for BDFIG operation is the synchronous mode in which the frequency of the induced voltage in the PW due to the cross-coupling with CW is equal to the frequency of the PW voltage source and vice versa. This necessitates the production of two fields by PW and CW rotating at the same electrical speed with respect to the rotor. Furthermore, due to the chosen number of rotor nests, the direction of rotation of the PW MMF with respect to the rotor should be opposite to the CW MMF to obtain cross-coupling, as shown in Fig. 3.

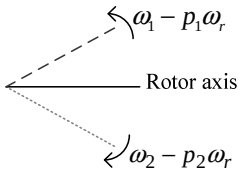

Fig. 3. Electrical speeds of two stator fields with respect to the rotor

In this situation [29],

$$\omega_1 - p_1\omega_r = -(\omega_2 - p_2\omega_r) \tag{4}$$

thus, the synchronous speed is determined as:

$$\omega_r = \frac{\omega_1 + \omega_2}{p_1 + p_2} \tag{5}$$

If the CW current is DC, the natural speed will be achieved [7] as:

$$\omega_n = \frac{\omega_1}{p_1 + p_2} \tag{6}$$

In this paper, the stator windings' MMFs are assumed to have sinusoidal distribution and core saturation effects are neglected. Considering only the p_1 and p_2 pole pair MMFs and neglecting other spatial harmonics in the air gap and also, using an equivalent impedance for the nested loop rotor, a dq model of the BDFIG in the p_1 pole pair synchronously rotating reference frame is obtained as [9]:

$$\psi_1 = L_1 i_1 + L_{1r} i_r \tag{7}$$

$$\psi_2 = L_2 i_2 + L_{2r} i_r \tag{8}$$

$$\psi_r = L_r i_r + L_{1r} i_1 + L_{2r} i_2 \tag{9}$$

$$v_1 = R_1 i_1 + \frac{d\psi_1}{dt} + j\omega_1 \psi_1 \tag{10}$$

$$v_2 = R_2 i_2 + \frac{d\psi_2}{dt} + j(\omega_1 - N_r\omega_r)\psi_2 \tag{11}$$

$$v_r = R_r i_r + \frac{d\psi_r}{dt} + j(\omega_1 - p_1\omega_r)\psi_r = 0 \tag{12}$$

$$T_e = -\frac{3}{2} p_1 \operatorname{Im}\left[\psi_1^* i_1\right] - \frac{3}{2} p_2 \operatorname{Im}\left[\psi_2 i_2^*\right] \tag{13}$$

However, the mechanical equation is:

$$T_m - T_e = J\frac{d\omega_r}{dt} + B\omega_r \tag{14}$$

The axis of the PW flux is selected as the d -axis reference under steady state conditions. This results in relatively independent controllability of rotor speed and PW reactive power by q and d axes of CW voltage, respectively [10], [12]. It is noteworthy that the reference value for the wind turbine rotor speed is determined to maximize the power captured from wind. The controllers of the rotor speed and PW reactive power are illustrated in Fig. 4. In these controllers, q components have higher priority. In other words:

$$\begin{aligned} &I_{2q\_sat} = I_{2-rated},\ V_{2q\_sat} = V_{2-rated} \\ &I_{2d\_sat} = \sqrt{I_{2-rated}^2 - I_{2q}^2},\ V_{2d\_sat} = \sqrt{V_{2-rated}^2 - V_{2q}^2} \end{aligned} \tag{15}$$

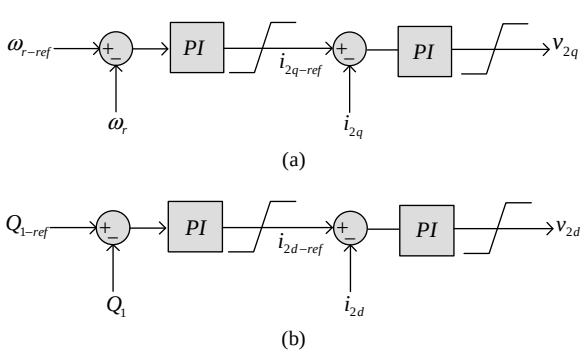

Fig. 4. The controllers for: (a) Rotor speed, (b) PW reactive power

III. Ride-through Analysis of BDFIG

A three phase voltage dip at the BDFIG terminals may occur due to some events in the power system, such as short

circuit or connection of large loads. Neglecting R_1 in (10) leads to an approximate relation for the PW flux during the transients resulting from a voltage dip, as stated in (16).

$$\psi_{1f} \approx \frac{V_{1-f}}{\omega_1} + \frac{V_{1-0} - V_{1-f}}{\omega_1} e^{-j\omega_1 t} e^{-\sigma t} \tag{16}$$

where σ is damping of the PW flux and depends on the PW resistance. If this equation is rewritten in the PW stationary reference frame, (17) will be obtained. Details of the transformation between different reference frames are given in [9].

$$\psi_{1f} \approx \frac{V_{1-f}}{\omega_1} e^{j\omega_1 t} + \frac{V_{1-0} - V_{1-f}}{\omega_1} e^{-\sigma t} \tag{17}$$

As can be observed, this flux is divided into two components. The first part is rotating synchronously and its amplitude is directly dictated by the remaining terminal voltage. The second component is DC and frozen with respect to the PW. Its amplitude is proportional to the voltage dip level and is exponentially damped during the fault. These flux components induce back EMFs in the rotor.

It is noteworthy that the speed of the first component with respect to the rotor is equal to $\omega_1 - p_1\omega_r$ and hence, the p_2 order harmonics of MMF produced by the rotor rotate with respect to the rotor at $p_1\omega_r - \omega_1$. Consequently, the rotational speed of this harmonic MMF with respect to the CW will be equal to $N_r\omega_r - \omega_1$, leading to an induced EMF in the CW with a frequency of $N_r f_r - f_1$. However, due to the decrease of amplitude of PW linkage flux first component during voltage dips, the EMF induced in CW with the frequency of $N_r f_r - f_1$ will have a lower value with respect to the pre-fault condition.

The second component rotates with respect to the rotor at the electrical speed of $-p_1\omega_r$. The harmonic MMF with p_2 pole pairs, produced by the rotor, will rotate at $p_1\omega_r$ with respect to the rotor. Hence, this harmonic MMF will rotate at $p_1\omega_r + p_2\omega_r$, or $N_r\omega_r$, with respect to the CW and consequently will lead to an induced EMF with frequency $N_r f_r$.

Combining (7)–(12) and (16) and neglecting rotor resistance, the CW voltage can be written as:

$$v_2 = R_2' i_2 + j(\omega_1 - N_r\omega_r)L_2' i_2 + L_2' \frac{di_2}{dt} + E_2' \tag{18}$$

$$R_2' = R_2 + \left(\frac{L_{1r}L_{2r}}{L_1L_r - L_{1r}^2}\right)^2 R_1 \tag{19}$$

$$L_2' = L_2 - \frac{L_1 L_{2r}^2}{L_1L_r - L_{1r}^2} \tag{20}$$

$$E_2' = \frac{1}{\omega_1}\frac{L_{1r}L_{2r}}{L_1L_r - L_{1r}^2}\left[\left(\frac{R_1L_r}{L_1L_r - L_{1r}^2} + j(N_r\omega_r - \omega_1)\right)V_{1-f} + \left(\frac{R_1L_r}{L_1L_r - L_{1r}^2} + jN_r\omega_r\right)(V_{1-0} - V_{1-f})e^{-\sigma t}e^{-j\omega_1 t}\right] \tag{21}$$

where R_2', L_2' and E_2' are the CW transient resistance, CW transient inductance and back EMF induced in CW during voltage dips, respectively.

By transforming (18) and (21) to the CW stationary reference frame, (22) and (23) are obtained, respectively. Then, the transient equivalent circuit seen from the CW can be drawn as Fig. 5.

$$v_2 = R_2' i_2 + L_2' \frac{di_2}{dt} + E_2' \tag{22}$$

$$E_2' = E_{2-1}' + E_{2-2}' = \frac{1}{\omega_1}\frac{L_{1r}L_{2r}}{L_1L_r - L_{1r}^2}\left[\left(\frac{R_1L_r}{L_1L_r - L_{1r}^2} - j(N_r\omega_r - \omega_1)\right)V_{1-f}e^{j(N_r\omega_r - \omega_1)t} + \left(\frac{R_1L_r}{L_1L_r - L_{1r}^2} - jN_r\omega_r\right)(V_{1-0} - V_{1-f})e^{-\sigma t}e^{jN_r\omega_r t}\right] \tag{23}$$

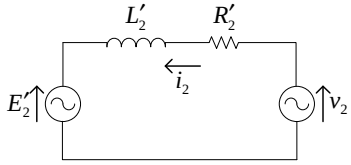

Fig. 5. Transient Equivalent Circuit of the CW

From (23), it can be observed that E_2' consists of two components with different frequencies, i.e. $N_r f_r - f_{12}$ and $N_r f_r$. As mentioned before, the amplitude of the first component depends on the voltage level at the generator terminals. But, the amplitude of the second component depends on the voltage dip and is damped with a factor related to R_1. However, assuming that the CW reaches its steady state condition during the fault, E_2' can similarly be calculated for post fault condition, as (24).

$$E_2' = E_{2-1}' + E_{2-2}' = \frac{1}{\omega_1}\frac{L_{1r}L_{2r}}{L_1L_r - L_{1r}^2}\left[\left(\frac{R_1L_r}{L_1L_r - L_{1r}^2} - j(N_r\omega_r - \omega_1)\right)V_{1-0}e^{j(N_r\omega_r - \omega_1)t} + \left(\frac{R_1L_r}{L_1L_r - L_{1r}^2} - jN_r\omega_r\right)(V_{1-f} - V_{1-0})e^{-\sigma t}e^{jN_r\omega_r t}\right] \tag{24}$$

Due to the unbalance between the induced transient EMFs in the CW and the MSI injected voltage, transient currents will appear in the CW. Furthermore, a DC component will exist with a time constant equal to L_2'/R_2', which is related to the natural frequency of the circuit in Fig. 5. These currents may be large enough to damage the MSI or the DC link capacitor. To overcome this problem, two solutions are proposed in the following section.

IV. Improvement of BDFIG Ride-through Capability

As mentioned in the previous section, large currents due to voltage dips may damage the converter. Hence, the generator

needs to be disconnected from the grid to protect the converter, despite the grid codes. In this section, two solutions are proposed to protect the converter without disconnecting the generator from the grid and thereby increasing the BDFIG low voltage ride-through capability.

A. Use of the crowbar

The first approach is to use crowbar resistors, connected across the CW terminals of the BDFIG and turn off the MSI (Fig. 6) in a similar way to what is normal practice on the DFIG. This will introduce a relatively high impedance circuit to the transient EMFs induced in the CW. The crowbar resistance should be high enough to provide sufficient damping for CW currents. On the other hand, a high resistance can generate high enough voltages to damage MSI switches. Hence, its maximum resistance should also be determined.

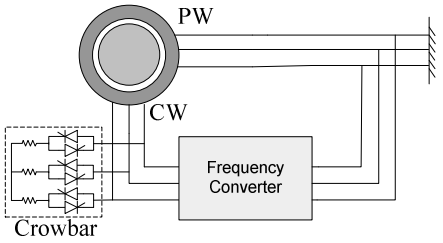

Fig. 6. BDFIG with crowbar

From (22)-(24), the CW current during and after a three phase voltage dip has a general form which is a summation of three terms as follows:

$$i_2 = k_1 e^{-\frac{R_2'}{L_2'}t} + k_2 e^{j(N_r\omega_r-\omega_1)t} + k_3 e^{-\sigma t} e^{jN_r\omega_r t} \tag{25}$$

Due to the rapid damping of the first term, it can be neglected. The highest possible voltage occurs when the latter two terms have simultaneous peaks. From (23) and (24) it is evident that E_2' will be greater after voltage recovery. Hence, the highest possible value after voltage recovery will be,

$$\max\{i_2\} = \max\left\{k_2 e^{j(N_r\omega_r-\omega_1)t} + k_3 e^{-\sigma t} e^{jN_r\omega_r t}\right\} =$$
$$\frac{\max\{E'_{2-1}\}}{\sqrt{(R_2'+R_{cr})^2+L_2'^2(N_r\omega_r-\omega_1)^2}} + \frac{\max\{E'_{2-2}\}}{\sqrt{(R_2'+R_{cr})^2+L_2'^2(N_r\omega_r)^2}}$$
$$\max\{E'_{2-1}\} = \frac{1}{\omega_1}\frac{L_{1r}L_{2r}}{L_1L_r-L_{1r}^2}\sqrt{\left(\frac{R_1L_r}{L_1L_r-L_{1r}^2}\right)^2+(N_r\omega_r-\omega_1)^2}V_{1-0} \tag{26}$$
$$\max\{E'_{2-2}\} = \frac{1}{\omega_1}\frac{L_{1r}L_{2r}}{L_1L_r-L_{1r}^2}\sqrt{\left(\frac{R_1L_r}{L_1L_r-L_{1r}^2}\right)^2+(N_r\omega_r)^2}(V_{1-0}-V_{1-f})$$

It should be noted that maximum instantaneous voltage tolerable by IGBT switches in the converter is usually considered to be 1.2 times the DC link voltage. Hence, the maximum crowbar resistance voltage drop obtained will be:

$$R_{cr}\left[\frac{\max\{E'_{2-1}\}}{\sqrt{(R_2'+R_{cr})^2+L_2'^2(N_r\omega_r-\omega_1)^2}} + \frac{\max\{E'_{2-2}\}}{\sqrt{(R_2'+R_{cr})^2+L_2'^2(N_r\omega_r)^2}}\right] < 0.7V_{C-rated} \tag{27}$$

From (27), the maximum crowbar resistance can be obtained in accordance with 100 % voltage dip, or minimum grid code, and the highest rotor speed.

It should be noted that the crowbar operation transforms BDFIG to a cascade machine and therefore the machine behavior becomes similar to an induction machine with N_r pole pairs [14]. Consequently, it absorbs reactive power in contrast to the grid code requirements [1] and further voltage reduction at generator terminals may occur.

B. Use of the series dynamic resistor

Another alternative is to increase the CW resistance during voltage dip by dynamic resistors connected in series with the CW, as illustrated in Fig. 7. The SDR is bypassed via high current, low voltage IGBTs under steady state conditions, and becomes active during voltage dips. In this manner, the SDR increases the CW resistance and consequently R_2'. Hence, the CW current peak decreases. Meanwhile, MSI is on and can affect the CW current to have a better control.

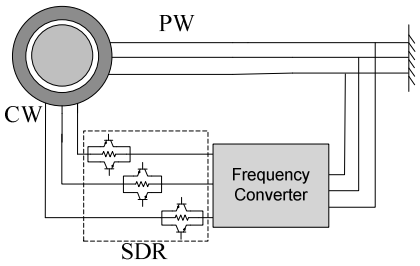

Fig. 7. BDFIG with SDR

The minimum SDR is determined to limit the CW maximum current to less than the maximum instantaneous current tolerable by the converter ($i_{2-\max}$), as (28).

$$\frac{\max\{E'_{2-1}\}}{\sqrt{(R_2'+R_{SDR})^2+L_2'^2(N_r\omega_r-\omega_1)^2}} + \frac{\max\{E'_{2-2}\}}{\sqrt{(R_2'+R_{SDR})^2+L_2'^2(N_r\omega_r)^2}} < i_{2-\max} \tag{28}$$

To derive (28), the MSI injected voltage is neglected. Practically, due to the use of a current limiter, the MSI voltage decreases the maximum current. Hence, neglecting this voltage increases the reliability margin of the resistance selection.

The crowbar and SDR should remain in circuit for a short period of time after voltage recovery to prevent current overshoots. It should be noted that the MSI cannot control the speed and reactive power until active power is accessible from the GSI via the DC link, which depends upon the terminal voltage as well as the DC link capacitance. However, every time MSI control is ineffective, the SDR will limit the CW current peaks, in a similar way to the crowbar. Clearly, the main drawback of the SDR is steady state loss in the switches.

V. VERIFICATION

A. Experimental validation of the model

An experimental set-up, shown in Fig. 8, was used to validate the simulation results. The delta-connected power winding of the BDFIG was connected to the grid through a variac and is supplied at rated voltage and frequency, i.e. $240\,V$ and $50\,Hz$ in normal conditions. The variac was manually changed to emulate a symmetrical voltage drop and fault clearance. As can be seen in Fig. 9(a), the resulting voltage drop took about $300\,ms$, slower than a typical grid fault but on a similar scale. The control winding was also connected in delta and supplied by a unidirectional converter.

When the BDFIG's operating speed was above the natural speed, the control winding was exporting power. In this case, the resistor bank was used to absorb this power. Additionally, a filter was connected between the converter output and the CW to eliminate components related to the converter's switching frequency. Note that due to existence of the parallel resistor bank, even when the variac was changing, the DC-link voltage remained constant at about 300 V. In a real wind turbine, the DC-link voltage would fluctuate during faults and hence, a DC-link protective circuit, such as a chopper, is used to prevent over voltages. Hence, the parallel resistor bank can operate like an efficient protective circuit for the DC link by sinking the additional active power flowing from the CW.

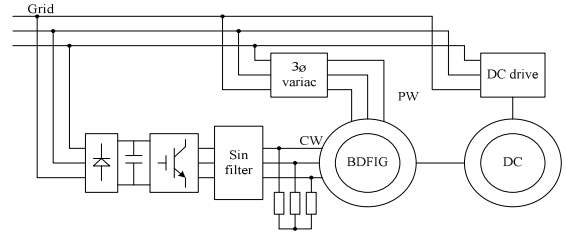

(a)

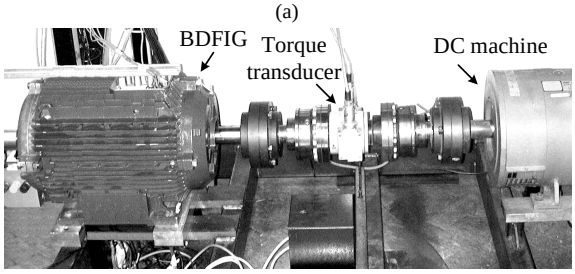

(b)

Fig. 8. (a) The test set up, (b) The BDFIG connected to a DC motor

The prototype BDFIG was coupled to a DC machine supplied from a commercial DC drive (ABB DCS800). The DC machine operates at constant speed and the BDFIG was in power control mode in normal conditions. An incremental encoder with 10,000 pulses per revolution was used to measure the shaft rotational speed. The control algorithm was implemented in MATLAB/Simulink in an xPC Target Box, which received all the above signals and generated PWM signals for the converter. The sampling time of the control loop was $0.4\,ms$.

The coupled-circuit model implemented for the prototype BDFIG-D180 was simulated using MATLAB/Simulink. The simulated machine parameters are presented in the Appendix. It should be noted that the model neglected iron loss and saturation. It also assumes fundamental sine wave excitation in the control winding. All the control parameters were kept the same as in the experiments.

The condition of a symmetrical voltage drop of about 50% in $300\,ms$ from $240\,V$ was considered. The BDFIG was operating at 20 Nm and 600 rpm before the fault occurred. The experimental and simulation results are illustrated in Fig. 9. As observed, the simulation results show a good similarity to the experimental ones. Therefore, it is observed that the coupled-circuit model is an acceptable tool for evaluating the BDFIG dynamic performance.

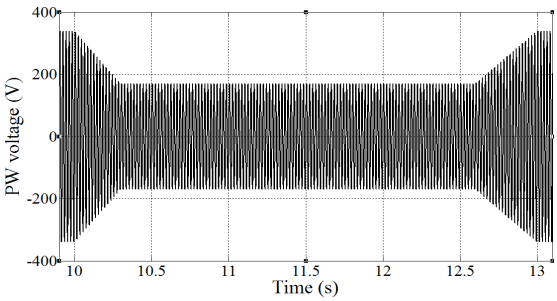

(a)

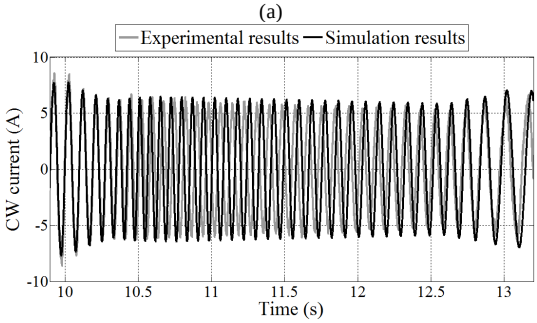

(b)

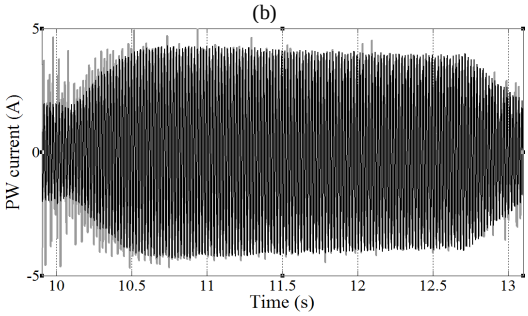

(c)

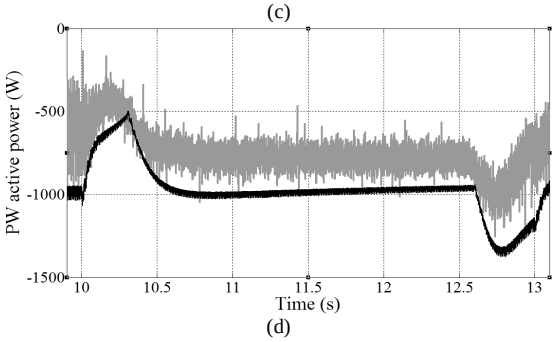

(d)

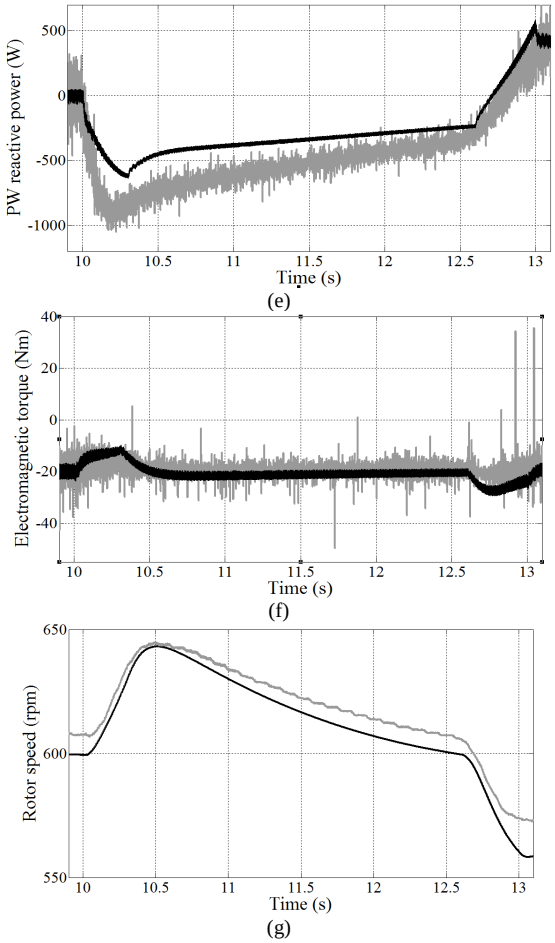

Fig. 9. Measurement and simulation results for D180 BDFIG: (a) The terminal voltage, (b) CW current, (c) PW current, (d) PW active power, (e) PW reactive power, (f) Electromagnetic torque and (g) Rotor speed

A. *Ride-through assessment*

In order to simulate the dynamic behavior of the machine during instantaneous voltage dips, the coupled-circuit model, which is more precise than *dq* model, was used. Initially, the simulation was performed for a 70% three phase voltage dip. However, in order to consider the effect of wind turbine inertia, J was considered equal to $3\,kgm^2$. The terminal voltage dip occurred at $t=10s$ and continued for $1000\,ms$. The variation of phase 'a' current of the CW with 50 Nm input torque and unity power factor at 600 rpm due to aforementioned voltage dip is shown in Fig. 10(a), (b).

As expected, two frequencies $N_r f_r - f_1 \approx 10Hz$ and $N_r f_r \approx 60Hz$ were observed in the initial instants after the voltage dip in Figs. 10(a) and (b), respectively. Furthermore, the second frequency component was damped with a time constant close to $0.15s$, as observed in Fig. 10(a). The CW current peak was less than the maximum permissible for the switches (16A) and therefore the generator does not need to be disconnected from the grid at this voltage dip and rotor speed. The rotor speed variation is shown in Fig. 10(c). Due to the mismatch the between input mechanical and output electrical powers, the rotor speed increased about $52\,rpm$ within 1 second and, started to decrease immediately after voltage recovery.

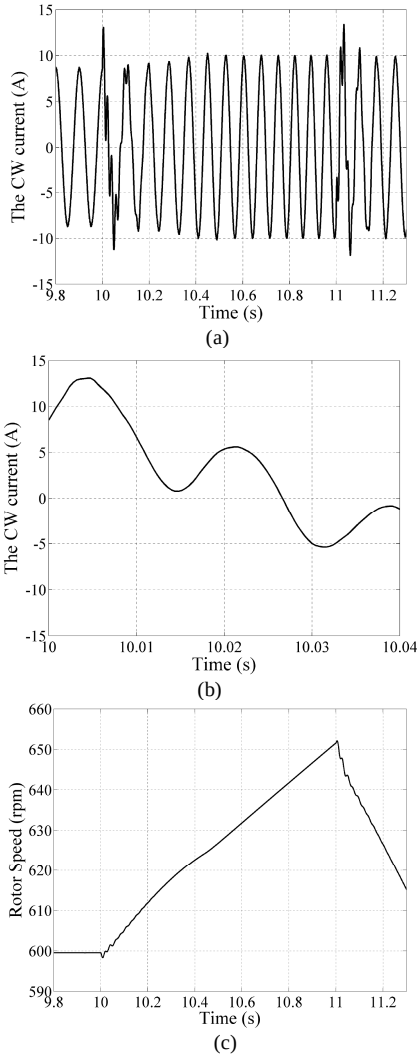

Fig. 10. Simulation results for D180 BDFIG due to 0.7 pu voltage dip from $t=10s$ to $t=11s$ at 600 rpm: (a) CW current, (b) CW current (zoomed in) and (c) Rotor speed

In order to obtain the region of feasibility for operation of the BDFIG-D180, the simulations were repeated with a voltage dip duration of $1000\,ms$ at $t=10s$ at various speeds and all with an input torque of 50 Nm and unity power factor. From these simulations, Fig. 11 is obtained for the maximum permissible CW current of $16\,A$. The area above the line (dotted) is the region of feasible operation, where instantaneous overshoot of the CW current remains under $16\,A$ both during and after the voltage dip. The area below the line (solid) is the region of unfeasible operation, where the CW current exceeds the 16A limit.

A. *Ride-through enhancement*

In general, the crowbar and SDR could be a set of series resistances with parallel switches. Thus, their effective resistance could be controlled in several steps in accordance with the voltage dip severity and pre-fault rotor speed.

However, in order to simplify the analysis, in this paper they have been considered as fixed resistances calculated for the worst case situation, i.e. 100% voltage dip and maximum rotor speed of 750 *rpm* , to guarantee safe operation of the converter switches in the case of any low voltage ride-through scenario. Hence, using (27) and (28), the crowbar and SDR resistances are obtained as $12.7\,\Omega$ and $21.5\,\Omega$, respectively. The peaks of the CW current with SDR and crowbar voltage due to 100% voltage dip are depicted in Fig. 12 and 13, respectively. From these results it can be concluded that by applying SDR and crowbar, the CW current and the voltage drop on the crowbar remain below their limits – 16 *A* and $274\,V$, respectively – for any voltage dip level and any pre-fault rotor speed up to 750 *rpm* .

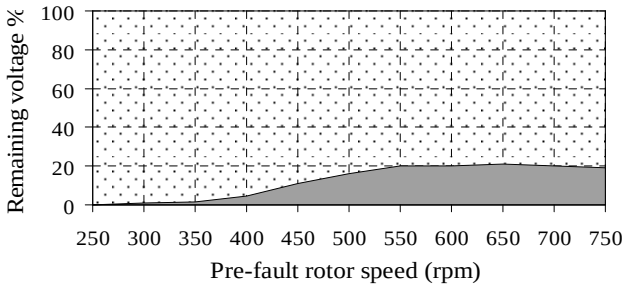

Fig. 11. Region of feasible operation for the D180 BDFIG ride-through

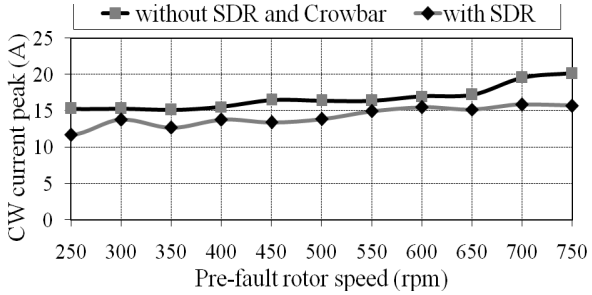

Fig. 12. CW current peak versus pre-fault rotor speed with 100% voltage dip

As an example, variations of the CW current, rotor speed, active and reactive powers in three cases of 85% voltage dip at 600 *rpm* from $t = 10s$ to $t = 11s$ with the use of either the crowbar or SDR and without them are illustrated in Fig. 14. The crowbar or SDR remained in circuit for a further 20 *ms* after voltage recovery to prevent high current peaks.

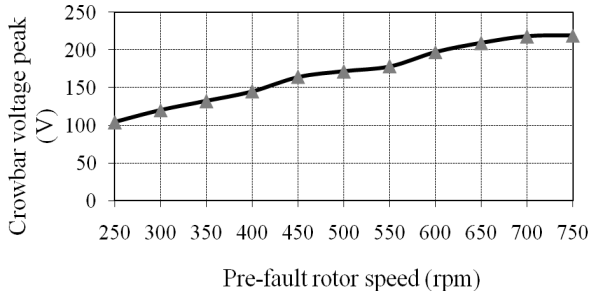

Fig. 13. Crowbar voltage peak versus pre-fault rotor speed with 100% voltage dip

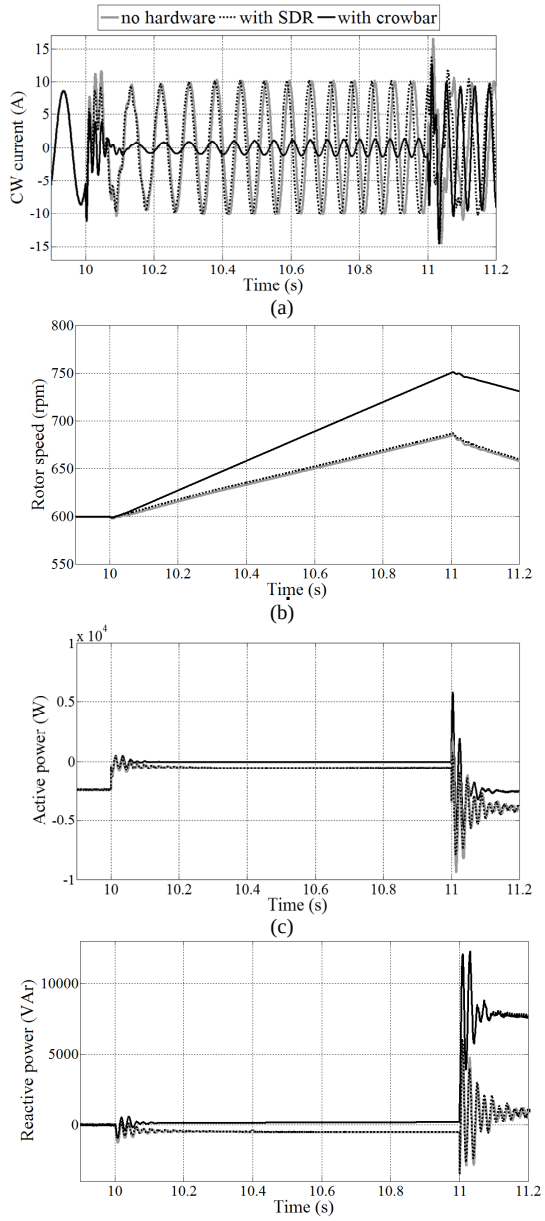

Fig. 14. Simulation results for D180 BDFIG due to 85% voltage dip at 600 *rpm* with the use of either SDR or crowbar: (a) CW phase current, (b) Rotor speed, (c) active power and (d) Reactive power

As observed, the use of SDR leads to better control of the active and reactive powers compared to the case where the crowbar is used. Using the crowbar leads to $60\,W$ export and $150\,VAr$ import during the voltage dip, whereas application of the SDR leads to both $540\,W$ and $500\,VAr$ export. Furthermore, significant difference between reactive power imports after voltage recovery clarifies further the advantage of the SDR. It should be noted that these results were obtained without modification during the voltage dips to the inverter controllers. Hence, the dynamic behavior of the SDR has the potential to be improved further

Fig. 15 shows the voltage drop across the crowbar and it can be observed that voltage remained below the acceptable limit ($274\,V$).

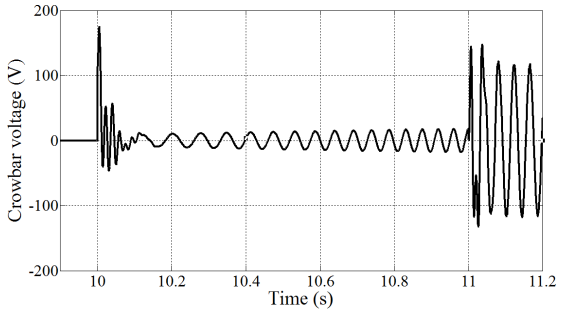

Fig. 15. Crowbar phase voltage variations due to 85% voltage dip at 600 *rpm*

VI. Conclusion

The structure and synchronous operation of BDFIG are introduced briefly in this paper. Variation of linkage fluxes and back electromotive forces are investigated analytically using the machine *dq* model in the p_1 pole pair synchronously rotating reference frame. The equivalent dynamic circuit of the CW is then obtained. The analysis shows that during or after a voltage dip, the EMF induced in the CW can be greater than its pre-fault value and consequently, high transient CW currents may appear.

Two approaches are suggested to overcome this problem; the use of crowbar, as has traditionally been the case with DFIG, or the use of SDR. Simple relations to determine appropriate values for both are proposed. First, the validity of the model used for simulation is checked by comparing simulation with experimental results on a D180 BDFIG. Then, the proposed solutions are implemented in simulations and their efficacy is explored. The results show that both the crowbar and SDR solutions develop a region of feasible voltage dip operation for the BDFIG up to maximum rotor speed.

While the use of crowbar provides more CW current damping, it leads to higher reactive power import. On the other hand, the use of SDR results in better control on active and reactive powers, but its conductive loss reduces the steady state efficiency.

Appendix

TABLE I
PROTOTYPE BDFIG SPECIFICATIONS

Parameter	Value	Parameter	Value
frame size	D180	f_1	$50\ Hz$
p_1	2	L_1	$0.3498\ H$
p_2	4	L_2	$0.3637\ H$
N_r	6	L_r	$0.044521\ mH$
stator slots	48	L_{1r}	$0.0031\ H$
rotor slots	36	L_{2r}	$0.0022\ H$
PW rated voltage	$240\ V$ (at $50\ Hz$)	R_1	$2.3\ \Omega$
CW rated voltage	$240\ V$ (at $50\ Hz$)	R_2	$4\ \Omega$
PW rated current	$8\ A$	R_r	$0.00012967\ \Omega$
CW rated current	$8\ A$	J	$0.53\ kgm^2$
rated torque	$50\ Nm$	B	$0.036\ Nms$

References

[1] Grid Connection Code - extra high voltage - Transpower stromübertragungs gmbh, April 2009, [On line] Available: http:// www.tennettso.de

[2] F. K. A. Lima, A. Luna, P. Rodriguez, E. H. Watanabe, F. Blaabjerg, "Rotor voltage dynamics in the doubly fed induction generator during grid faults", *IEEE Transaction on Power Electronics*, Vol. 25, No. 1, Jan 2010, pp. 118-130

[3] H. Arabian-Hoseynabadi, H. Oraee, and P.J. Tavner, "Failure modes and effects analysis (FMEA) for wind turbines", *International Journal of Electrical Power & Energy Systems*, Vol. 32, No. 7, Sep 2010, pp. 817-824

[4] L. Gertmar, "A constant-frequency machine with a varying/variable speed", Canadian Intellectual Property Office 2 367 389, Nov 9, 2000

[5] R. A. McMahon, P.C. Roberts, X. Wang, and P. J. Tavner, "Performance of BDFM as generator and motor", *IEE Proceedings - Electric Power Applications*, Vol. 153, No. 2, Mar 2006, pp. 289- 299

[6] M. S. Boger, A. K. Wallace, and R. Spee, "Investigation of appropriate pole number combinations for brushless doubly fed machines applied to pump drives", *IEEE Transactions on Industry Applications*, Vol. 32, No. 1, Jan-Feb 1996, pp.189-194

[7] P. C. Roberts, R. A. McMahon, P. J. Tavner, J. M. Maciejowski, and T. J. Flack, "Equivalent circuit for the brushless doubly fed machine (BDFM) including parameter estimation and experimental verification", *IEE Proceedings - Electric Power Applications*, Vol. 152, No. 4, Jul 2005, pp. 933- 942

[8] D. Zhou, R. Spee, and G. C. Alexander, "Experimental evaluation of a rotor flux oriented control algorithm for brushless doubly-fed machines", *IEEE Transactions on Power Electronics*, Vol. 12, No. 1, Jan 1997, pp.72-78

[9] J. Poza, E. Oyarbide, D. Roye, and M. Rodriguez, "Unified reference frame dq model of the brushless doubly fed machine", *IEE Proceedings - Electric Power Applications*, Vol. 153, No. 5, Sep 2006, pp. 726-734

[10] J. Poza, E. Oyarbide, I. Sarasola, and M. Rodriguez, "Vector control design and experimental evaluation for the brushless doubly fed machine", *IET Electric Power Applications*, Vol. 3, No. 4, Jul 2009, pp. 247-256

[11] S. Shao, E. Abdi, and R. McMahon, "Low-cost variable speed drive based on a brushless doubly-fed motor and a fractional unidirectional converter", *IEEE Transaction on Industrial Electronics*, Vol. 59, No. 1, Jan 2012, pp. 317-325

[12] S. Shao, E. Abdi, F. Barati, and R. McMahon, "Stator-flux-oriented control for brushless doubly fed induction generator", *IEEE Transaction on Industrial Electronics*, Vol. 56, No. 10, Oct 2009, pp. 4220-4228

[13] F. Barati, S. Shao, E. Abdi, H. Oraee, and R. McMahon, "Generalized vector model for the brushless doubly-fed machine with a nested loop rotor", *IEEE Transaction on Industrial Electronics*, Vol. 58, No. 6, Jun 2011, pp. 2313-2321

[14] P. C. Roberts, *A Study of Brushless Doubly Fed (Induction) Machines*, Ph.D. dissertation, Emanuel College, University of Cambridge, Cambridge, Sep 2004

[15] A. Mullane, G. Lightbody, and R. Yacamini, "Wind-turbine fault ride-through enhancement", *IEEE Transaction on Power Systems*, Vol. 20, No. 4, Nov 2005, pp. 1929- 1937

[16] M. Rahimi, and M. Parniani, "Transient performance improvement of wind turbines with doubly fed induction generators using nonlinear control strategy", *IEEE Transaction on Energy Conversion*, Vol. 25, No. 2, Jun 2010, pp. 514-525

[17] S. Alepuz, S. Busquets-Monge, J. Bordonau, J. A. Martinez-Velasco, C.A. Silva, J. Pontt, and J. Rodriguez, "Control Strategies Based on Symmetrical Components for Grid-Connected Converters Under voltage Dips", *IEEE Transaction on Industrial Electronics*, Vol. 56, No. 6, Jun 2009, pp. 2162-2173

[18] J. P. da Costa, H. Pinheiro, T. Degner, and G. Arnold, "Robust controller for DFIGs of grid-connected wind turbines", *IEEE Transaction on Industrial Electronics*, Vol. 58, No. 9, Sep 2011, pp. 4023-4038

[19] M. Molinas, J. A. Suul, and T. Undeland, "Low voltage ride through of wind farms with cage generators: STATCOM versus SVC", *IEEE Transaction on Power Electronics*, Vol. 23, No. 3, May 2008, pp. 1104-1117

[20] C. Abbey, and G. Joos, "Supercapacitor energy storage for wind energy applications", *IEEE Transaction on Industry Applications*, Vol. 43, No. 3, May-Jun 2007, pp. 769-776

[21] P. S. Flannery, and G. Venkataramanan, "Unbalanced voltage sag ride-through of a doubly fed induction generator wind turbine with series grid-side converter", *IEEE Transaction on Industry Applications*, Vol. 45, No. 5, Sep-Oct 2009, pp. 1879-1887

[22] A. H. Kasem, E. F. El-Saadany, H. H. El-Tamaly, and M. A. A. Wahab, "An improved fault ride-through strategy for doubly fed induction generator-based wind turbines", *IET Renewable Power Generation*, Vol. 2, No. 4, Dec 2008, pp. 201-214

[23] S. M. Muyeen, R. Takahashi, T. Murata, J. Tamura, M. H. Ali, Y. Matsumura, A. Kuwayama, and T. Matsumoto, "Low voltage ride through capability enhancement of wind turbine generator system during network disturbance", *IET Renewable Power Generation*, Vol. 3, No. 1, Mar 2009, pp. 65-74

[24] J. Yang, J. E. Feltcher, and J. O'Reilly, "A series-dynamic-resistor-based converter protection scheme for doubly-fed induction generator during various fault conditions", *IEEE Transaction on Energy Conversion*, Vol. 25, No. 2, Jun 2010, pp. 422-432

[25] D. Ramirez, S. Martinez, C. A. Platero, F. Blazquez, and R. M. de Castro, "Low-voltage ride-through capability for wind generators based on dynamic voltage restorers", *IEEE Transaction on Energy Conversion*, Vol. 26, No. 1, Mar 2011, pp. 195-203

[26] C. Wessels, F. Gebhardt, and F. W. Fuchs, "Fault ride-through of a DFIG wind turbine using a dynamic voltage restorer during symmetrical and asymmetrical grid faults", *IEEE Transactions on Power Electronics*, Vol. 26, No. 3, Mar 2011, pp. 807-815

[27] A. Luna, F. K. de A. Lima, D. Santos, P. Rodríguez, E. H. Watanabe, and S. Arnaltes, "Simplified modeling of a DFIG for transient studies in wind power applications", *IEEE Transactions on Industrial Electronics*, Vol. 58, No. 1, Jan 2011, pp. 9-20

[28] S. Shao, E. Abdi, and R. McMahon, "Dynamic analysis of the brushless doubly-fed induction generator during symmetrical three-phase voltage dips", *International Conference on Power Electronics and Drive Systems (PEDS*) 2009, Nov 2009, pp. 464-469

[29] S. Williamson, A. C. Ferreira, and A.K. Wallace, "Generalised theory of the brushless doubly-fed machine. I. Analysis", *IEE Proceedings - Electric Power Applications*, Vol. 144, No. 2, Mar 1997, pp. 111-122

VII. BIOGRAPHIES

Sajjad Tohidi was born in Meshkin Shahr, Iran, in 1984. He received the B.Sc. degree from Iran University of Science and Technology (IUST), Tehran, Iran, in 2006, and M.Sc. degree from Sharif University of Technology (SUT), Tehran, Iran, in 2008, both in Electrical Engineering. He is currently pursuing the Ph.D. program at SUT. He was on sabbatical at Durham University and University of Cambridge, both in UK in 2011. His research interests include power systems dynamics, electrical machines and wind power generation.

Hashem Oraee received a First Class Honours B.Eng degree in Electrical and Electronic Engineering from University of Wales, Cardiff, UK in 1980 and a PhD degree in Electrical Machines from University of Cambridge, UK in 1984. He is currently a professor of Electrical Engineering at Sharif University of Technology in Iran. His research interests include electrical energy conversion and power quality. He is also active in commercialization of Brushless Doubly Fed Induction Generators in wind generation industry.

Mohammad Reza Zolghadri received the B.Sc. and M.Sc. degrees from Sharif University of Technology, Tehran, Iran, in 1989 and 1992, respectively, and the Ph.D. degree from the Institute National Polytechnique de Grenoble, Grenoble, France, in 1997, all in electrical engineering. Since 1997, he has been with the College of Electrical Engineering, Sharif University of Technology. From 2000 to 2003, he was a Senior Researcher in the Electronics Laboratory, SAM Electronics Company, Tehran. His current research interests include application of power electronics in energy systems, and modeling and control of power electronic converters.

Shiyi Shao received the B.Eng. and M.Phil. degrees from Shanghai Jiao Tong University, Shanghai, China, in 2003 and 2006, respectively, and the M.Phil. and Ph.D. degrees in electrical engineering from Cambridge University, Cambridge, U.K., in 2008 and 2010, respectively. He is currently with Wind Technologies, Cambridge, involved in electrical system design and machine control. He is also working as a Research Collaborator at Cambridge University in the field of electrical machines, machine drive, and control.

Peter Tavner is Emeritus Professor at Durham University. Receiving an MA and PhD from Cambridge & Southampton Universities respectively he has held senior manufacturing industry positions, including Group Technical Director of FKI Energy Technology. Joining the University in 2003 he has been Principal Investigator of the Supergen Wind Consortium. He is President of European Academy of Wind Energy, Non-Exec Director of Wind Technologies and winner of the IET Institution Premium.